Isogeometric Analysis: new stable elements for the Stokes equation

A. Buffa * C. de Falco† G. Sangalli‡

February 2, 2010

Abstract

In this paper we discuss the application of IsoGeometric Analysis to incompressible viscous flow problems, for which preliminary results were presented in [1, 2, 3]. Here we consider, as a prototype problem, the Stokes system and we propose various choices of compatible Spline spaces for the approximations to the velocity and pressure fields. The proposed choices can be viewed as extensions of the Taylor-Hood, Nédélec and Raviart-Thomas pairs of finite element spaces, respectively. We study the stability and convergence properties of each method and discuss the conservation properties of the discrete velocity field in each case.

1 INTRODUCTION

The concept of Isogeometric Analysis (IGA) was introduced in [4] with the aim of bridging the gap between computer aided design (CAD) and the finite element method. This aim is pursued by adopting the same spline or Non Uniform Rational B-spline (NURBS) basis functions used to design domain geometries in CAD to construct both trial and test spaces in the discrete variational formulation of differential problems. As an additional benefit with respect to standard finite elements, the use of these functions allows to construct finite dimensional spaces of higher regularity. In this paper we discuss the application of IGA to incompressible viscous flow problems, for which preliminary results were presented in [1, 2, 3]. Here we consider, as a prototype problem, the Stokes system modeling the flow of a viscous, incompressible fluid with constant viscosity μ:

$$\left\{ \begin{array}{rl} -\mu\, \boldsymbol{\nabla}^2 \mathbf{u} + \boldsymbol{\nabla} p &= \mathbf{f} \quad \text{in } \Omega \\ \boldsymbol{\nabla} \cdot \mathbf{u} &= 0 \quad \text{in } \Omega \end{array} \right. \tag{1}$$

completed by suitable boundary conditions. In (1), $\mathbf{f} \in L^2(\Omega)^2$ and $\Omega \subset \mathbb{R}^2$ is the image of the domain $\widehat{\Omega} = (0,1)^2$ under a *geometrical mapping* $\mathbf{F}$ that is *piecewise smooth* and has piecewise smooth inverse. In the following, $\widehat{\Omega}$ will be referred to as the *parametric domain* while Ω will be referred to as the *physical domain*.

We consider mixed variational discretizations of (1), in which an approximation $(\mathbf{u}_h, p_h)$ to the exact solution $(\mathbf{u}, p)$ of (1) is obtained by solving the problem:

$$a(\mathbf{u}_h, \mathbf{v}) + b(\mathbf{v}, p_h) = \int_\Omega \mathbf{f} \cdot \mathbf{v} \qquad \forall \mathbf{v} \in V_h, \tag{2a}$$

$$b(q, \mathbf{u}_h) = 0 \qquad \forall q \in Q_h, \tag{2b}$$

*Istituto di Matematica Applicata e Tecnologie Informatiche (IMATI) del CNR, via Ferrata, 1, 27100, Pavia, Italy
†Istituto di Matematica Applicata e Tecnologie Informatiche (IMATI) del CNR, via Ferrata, 1, 27100, Pavia, Italy
‡Dipartimento di Matematica, Università di Pavia via Ferrata 1, 27100, Pavia (Italy)

where (V_h, Q_h) are couples of finite dimensional spaces parametrized with h and the bilinear forms $a(\cdot,\cdot)$ and $b(\cdot,\cdot)$ are defined as

$$a(\mathbf{u},\mathbf{v}) = \int_\Omega \mu \boldsymbol{\nabla}\mathbf{u} : \boldsymbol{\nabla}\mathbf{v} \quad \text{and} \quad b(\mathbf{v},q) = -\int_\Omega q \ \text{div}\ \mathbf{v},$$

respectively.

In order to garantee stability, we consider only choices of discrete spaces that are *inf-sup stable*, *i.e.*, that satisfy the condition (see e.g., [5])

$$\inf_{q\in Q_h, q\neq 0} \sup_{\mathbf{v}\in V_h, \mathbf{v}\neq 0} \frac{b(\mathbf{v},q)}{\|q\|_{L^2}\|\mathbf{v}\|_{H^1}} \geq c_{is} > 0 \tag{3}$$

where c_{is} is independent of the parameter h. The discrete velocity $\mathbf{u}_h$ of the solution of (2) is, in general, not exactly divergence–free. A sufficient condition that guarantees divergence-free velocities is

$$Q_h \supseteq \{\, \text{div}\, \mathbf{v} \colon \mathbf{v} \in V_h \}\,, \tag{4}$$

which is in conflict with (3), unless the equality holds in (4). Discretization techniques that produce an exactly divergence–free velocity field are of great practical interest (see *e.g.* [6, 7]) and are not easy to devise in the framework of classical finite elements (see *e.g.* [8, 9]). In the context of Isogeometric Analysis, we present a few choices of spline based spaces (V_h, Q_h) which satify (3). The new elements we introduce can be seen as spline generalization of well known finite elements spaces, namely Taylor-Hood elements [10], Nédélec elements of the second family [11] and Raviart-Thomas elements [12]. Thanks to the high interelement regularity, which is the main feature of splines, all the proposed discretization are conforming, i.e., produce globally continuous discrete velocities. Moreover, the spline generalization of Raviart-Thomas elements enjoys also property (4) and thus provides divergence-free discrete solutions.

The outline of the paper is as follows. In Section 2 we introduce B-splines basis functions in one and two dimensions. In Section 3 we introduce our spline-based discrete spaces for the Stokes system and we discuss their main features. Finally, Section 4 is devoted to numerical testing.

2 B-SPLINES AND PIECE-WISE SMOOTH FUNCTIONS

2.1 B-spline spaces and piece-wise smooth functions in one dimension

Given positive integers p and n, such that $n \geq p+1$, we introduce the ordered knot vector

$$\Xi := \{0 = \xi_1, \xi_2, \ldots, \xi_{n+p+1} = 1\}\,, \tag{5}$$

where we allow repetitions of knots, that is, we assume $\xi_1 \leq \xi_2 \leq \cdots \leq \xi_{n+p+1}$. In the following we will only work with *open* knot vectors, which means that the first $p+1$ knots in Ξ are equal to 0, and the last $p+1$ are equal to 1, and we assume that all internal knots have multiplicity r, $1 \leq r \leq p+1$, so that

$$\Xi = \{\underbrace{\zeta_1, \ldots, \zeta_1}_{p+1 \text{ times}}, \underbrace{\zeta_2, \ldots, \zeta_2}_{r \text{ times}}, \ldots, \underbrace{\zeta_m, \ldots, \zeta_m}_{p+1 \text{ times}}\}.$$

The vector

$$\mathcal{Z} = \{0 = \zeta_1, \zeta_2, \ldots, \zeta_m = 1\}$$

represents the (ordered) vector of knots without repetitions, and the relation $m = \frac{n-p-1}{r} + 2$ holds.

Through the iterative procedure detailed in [4] we construct p-degree (that is, $(p+1)$-order) B-spline basis functions, denoted by B_i, for $i = 1, \ldots, n$. These basis functions are piecewise polynomials of degree p on the subdivision $\{\zeta_1, \ldots, \zeta_m\}$. At ζ_i they have $\alpha := p - r$ continuous derivatives. Therefore, $-1 \leq \alpha \leq p-1$: the maximum multiplicity allowed, $r = p+1$, gives $\alpha = -1$, which stands for

a discontinuity at each ζ_i. Each basis function B_i is non-negative and supported in the interval $[\xi_i, \xi_{i+p+1}]$. Moreover, these B-spline functions constitute a partition of unity, that is

$$\sum_{i=1}^{n} B_i(x) = 1 \quad \forall x \in (0,1). \tag{6}$$

The space of B-splines spanned by the basis functions B_i will be denoted by

$$S_\alpha^p := \text{span}\{B_i\}_{i=1}^n. \tag{7}$$

Derivatives of splines are splines as well. Let $S_{\alpha+1}^{p+1}$ and S_α^p be spline spaces constructed, according with the notation above, on the same subdivision $\{\zeta_1, \ldots, \zeta_m\}$. Then, it is easy to see that

$$\left\{ \frac{d}{dx} v : v \in S_{\alpha+1}^{p+1} \right\} = S_\alpha^p, \tag{8}$$

Notice moreover that

$$\# S_\alpha^p = p + 1 + (m-2)(p-\alpha), \tag{9}$$

and

$$\# S_{\alpha+1}^{p+1} = p + 2 + (m-2)(p-\alpha), \tag{10}$$

where # is used to denote the dimension of the linear space. Then, from (9)–(10), $\# S_{\alpha+1}^{p+1} = \# S_\alpha^p + 1$, in agreement with the fact that the derivative is a surjective operator from $S_{\alpha+1}^{p+1}$ to S_α^p and has a one-dimensional kernel, the constants.

We denote by $\mathcal{C}_\alpha^\infty$ the space of piecewise smooth functions on $(0,1)$, whose restriction to each subinterval (ζ_i, ζ_{i+1}) admits a C^∞ extension to the closed interval $[\zeta_i, \zeta_{i+1}]$ with α continuous derivatives at ζ_i, for all $i = 2, \ldots, m-1$.

2.2 B-spline spaces and piece-wise smooth functions in two dimensions

The definition of B-splines spaces given above can be extended to two dimensions as follows. Let us consider the square $\widehat{\Omega} = (0,1)^2 \subset \mathbb{R}^2$, which will be referred to as *parametric domain*. Given integers p_d, r_d, n_d and $\alpha_d = p_d - r_d$, with $d = 1, 2$, we introduce the knot vectors $\Xi_d = \{\xi_{1,d}, \xi_{2,d}, \ldots, \xi_{n_d+p_d+1,d}\}$ and the associated vectors $\mathcal{Z}_d = \{\zeta_{1,d}, \ldots, \zeta_{m_d,d}\}$ as in the one-dimensional case. Associated with these knot vectors there is a *mesh* $\mathcal{Q}_h$ of the parametric domain, that is, a partition of $(0,1)^2$ into rectangles:

$$\mathcal{Q}_h = \{Q = \otimes_{d=1,2}(\zeta_{i_d,d}, \zeta_{i_d+1,d}),\ 1 \le i_d \le m_d - 1\}. \tag{11}$$

Given an element $Q \in \mathcal{Q}_h$, we set $h_Q = \text{diam}(Q)$, and define the global mesh size $h = \max\{h_Q,\ Q \in \mathcal{Q}_h\}$. We associate to the two given knot vectors Ξ_d, $d = 1, 2$ the p_d-degree univariate B-splines basis functions $B_{i,d}$, with $i = 1, \ldots, n_d$. Then, on the associated mesh $\mathcal{Q}_h$, we define the tensor-product B-spline basis functions as

$$B_{ij} := B_{i,1} \otimes B_{j,2}, \quad i = 1, \ldots, n_1,\ j = 1, \ldots, n_2\,. \tag{12}$$

Then, the tensor product B-spline space is defined as the space spanned by these basis functions, namely

$$S_{\alpha_1,\alpha_2}^{p_1,p_2} \equiv S_{\alpha_1,\alpha_2}^{p_1,p_2}(\mathcal{Q}_h) := S_{\alpha_1}^{p_1} \otimes S_{\alpha_2}^{p_2} = \text{span}\{B_{ij}\}_{i=1,j=1}^{n_1,n_2}\,. \tag{13}$$

Notice that the space $S_{\alpha_1,\alpha_2}^{p_1,p_2}(\mathcal{Q}_h)$ is fully characterized by the mesh $\mathcal{Q}_h$, by p_1, p_2, α_1 and α_2, as our notation reflects. The minimum regularity of the space is $\alpha := \min\{\alpha_d :\ d = 1, 2\}$.

In a similar way, we define on $\mathcal{Q}_h$ the space of piecewise smooth functions with interelement regularity on the vertical and horizontal mesh edges given by α_1 and α_2 respectively. This is denoted by

$$\mathcal{C}_{\alpha_1,\alpha_2}^\infty = \mathcal{C}_{\alpha_1,\alpha_2}^\infty(\mathcal{Q}_h) = \mathcal{C}_{\alpha_1}^\infty \otimes \mathcal{C}_{\alpha_2}^\infty.$$

Precisely, a function in $\mathcal{C}^{\infty}_{\alpha_1,\alpha_2}$ admits a C^∞ extension in the closure of each element $Q \in \mathcal{Q}_h$, has α_1 continuous derivatives on the edges $\{(x_1, x_2) : x_1 = \zeta_{i,1}, \zeta_{j,2} < x_2 < \zeta_{j+1,2}\}$, for $j = 1, \ldots, m_2 - 1$, $i = 2, \ldots, m_1 - 1$ and α_2 continuous derivatives on the edges $\{(x_1, x_2) : \zeta_{j,1} < x_1 < \zeta_{j+1,1}, x_2 = \zeta_{i,2}, \}$, for $j = 1, \ldots, m_1 - 1$, $i = 2, \ldots, m_2 - 1$. From the definitions, $S^{p_1,p_2}_{\alpha_1,\alpha_2} \subset \mathcal{C}^{\infty}_{\alpha_1,\alpha_2}$.

From an initial coarse mesh $\mathcal{Q}_{h_0}$, refinements are constructed by knot insertion (with possible repetition, see [13]). Therefore, we end up considering a family of meshes $\{\mathcal{Q}_h\}_{h \le h_0}$ and associated spaces, with the global mesh size h playing the role of family index, as usual in finite element literature.

We assume that our computational domain $\Omega \subset \mathbb{R}^2$ can be exactly parametrized by a geometrical mapping $\mathbf{F} : \widehat{\Omega} \longrightarrow \Omega$ which belongs to $(\mathcal{C}^{\infty}_{\gamma_1,\gamma_2}(\mathcal{Q}_h))^2$, with piecewise smooth inverse, and is independent of the mesh family index h. The global regularity of $\mathbf{F}$ is $\gamma := \min\{\gamma_d : d = 1, 2\}$.

3 DISCRETIZATION OF THE VECTOR FIELDS

3.1 Spline spaces on the parametric domain

Given the two (horizontal and vertical) knot vectors, $\mathcal{Z}_1 = \{\zeta_{1,1}, \ldots, \zeta_{m_1,1}\}$ and $\mathcal{Z}_2 = \{\zeta_{1,2}, \ldots, \zeta_{m_2,2}\}$, and the associated mesh $\mathcal{Q}_h$ on the parametric domain $\widehat{\Omega}$, we introduce the following pairs of velocity-pressure spaces:

$$\widehat{V}_h^{\mathrm{RT}} \equiv \widehat{V}_h^{\mathrm{RT}}(p,\alpha) = S^{p+1,p}_{\alpha+1,\alpha}(\mathcal{Q}_h) \times S^{p,p+1}_{\alpha,\alpha+1}(\mathcal{Q}_h); \qquad \widehat{Q}_h^{\mathrm{RT}} \equiv \widehat{Q}_h^{\mathrm{RT}}(p,\alpha) = S^{p,p}_{\alpha,\alpha}(\mathcal{Q}_h); \tag{14a}$$

$$\widehat{V}_h^{\mathrm{N}} \equiv \widehat{V}_h^{\mathrm{N}}(p,\alpha) = S^{p+1,p+1}_{\alpha+1,\alpha}(\mathcal{Q}_h) \times S^{p+1,p+1}_{\alpha,\alpha+1}(\mathcal{Q}_h); \qquad \widehat{Q}_h^{\mathrm{N}} \equiv \widehat{Q}_h^{\mathrm{N}}(p,\alpha) = S^{p,p}_{\alpha,\alpha}(\mathcal{Q}_h); \tag{14b}$$

$$\widehat{V}_h^{\mathrm{TH}} \equiv \widehat{V}_h^{\mathrm{TH}}(p,\alpha) = S^{p+1,p+1}_{\alpha,\alpha}(\mathcal{Q}_h) \times S^{p+1,p+1}_{\alpha,\alpha}(\mathcal{Q}_h); \qquad \widehat{Q}_h^{\mathrm{TH}} \equiv \widehat{Q}_h^{\mathrm{TH}}(p,\alpha) = S^{p,p}_{\alpha,\alpha}(\mathcal{Q}_h). \tag{14c}$$

The first velocity space, $\widehat{V}_h^{\mathrm{RT}}$, when $\alpha = -1$, represents the classical Raviart-Thomas element [12, 5], while $\widehat{V}_h^{\mathrm{N}}$, still for $\alpha = -1$, gives the Nédélec element of second kind [14, 11]. However these are both discontinuous discrete spaces, that is, they do not give an H_0^1-conforming discretization of the velocity field. For that reason classical (discontinuous) Raviart-Thomas and Nédélec elements are not popular in the finite element approximations of the Stokes problem, since they lead to non-conforming schemes, though interesting results are proposed in [15, 9, 16]. Here, we are primarily interested to conforming discretizations, therefore we assume $0 \le \alpha \le p - 1$. The pair $\widehat{V}_h^{\mathrm{RT}}(2,0) \times \widehat{Q}_h^{\mathrm{RT}}(2,0)$ has been proposed in [17] and [18].

The third pair of spaces (14c) corresponds to the Taylor-Hood elements [10] for $\alpha = 0$. These are instead very popular in the finite element literature for the Stokes problem. In this context, we can have smoother discretizations, that is we still allow $0 \le \alpha \le p - 1$.

Observe that given p and α, the pressure spaces in (14a)–(14c) are the same, while for the velocity spaces $\widehat{V}_h^{\mathrm{RT}} \subset \widehat{V}_h^{\mathrm{N}} \subset \widehat{V}_h^{\mathrm{TH}}$ holds.

There is numerical evidence that the inf-sup condition for the pairs in (14a)–(14c) holds uniformly with respect to h. The results of numerical inf-sup tests are shown for $p = 3$ and $\alpha = 2$ in Table 1. Stability of the pairs (14b)–(14c) is mantained if we impose no-slip Dirichlet boundary conditions on the velocity space, and a zero mean-value constraint on the pressure space, see Table 2. Pair (14a) becomes unstable when no-slip boundary conditions are imposed: this issue will be addressed in the next section where two possible remedies are proposed.

3.2 On the $\widehat{V}_h^{\mathrm{RT}}$ space

We now discuss a particular and interesting feature of the pair $\widehat{V}_h^{\mathrm{RT}} \times \widehat{Q}_h^{\mathrm{RT}}$. In the following Theorem we characterize the range of the div operator in the situations of interest.

h	1/8	1/12	1/16	1/20	1/24	1/28	1/32
c_{is}^{RT}	0.879	0.883	0.884	0.884	0.884	0.884	0.884
c_{is}^{N}	0.971	0.972	0.973	0.973	0.973	0.973	0.973
c_{is}^{TH}	0.995	0.995	0.995	0.995	0.995	0.995	0.995

Table 1: inf-sup test constant c_{is} on the parametric domain for the spaces (14a)–(14c), with $p = 3$ and $\alpha = 2$, without boundary conditions

h	1/8	1/12	1/16	1/20	1/24	1/28	1/32
c_{is}^{RT}	1.83e-08	5.24e-07	3.25e-09	4.03e-07	3.36e-07	1.26e-08	1.28e-08
c_{is}^{N}	0.454	0.451	0.449	0.448	0.447	0.446	0.446
c_{is}^{TH}	0.459	0.456	0.453	0.452	0.451	0.45	0.449

Table 2: inf-sup test constant c_{is} on the parametric domain for the spaces (14a)–(14c), with $p = 3$ and $\alpha = 2$, and with no-slip Dirichlet boundary conditions

Theorem 3.1 *Making use of the notation introduced above, for any $\mathcal{Q}_h$ and $p \geq 1$, $0 \leq \alpha \leq p-1$, we have*

$$\left\{ \operatorname{div} \mathbf{v} \,:\, \mathbf{v} \in \widehat{V}_h^{\mathrm{RT}} \right\} = \widehat{Q}_h^{\mathrm{RT}}, \tag{15}$$

$$\left\{ \operatorname{div} \mathbf{v} \,:\, \mathbf{v} \in \widehat{V}_h^{\mathrm{RT}} \text{ and } \mathbf{v} \cdot \mathbf{n}\,|_{\partial\widehat{\Omega}} = 0 \right\} = \left\{ q \in \widehat{Q}_h^{\mathrm{RT}} : \int_{\widehat{\Omega}} q = 0 \right\}, \tag{16}$$

$$\left\{ \operatorname{div} \mathbf{v} \,:\, \mathbf{v} \in \widehat{V}_h^{\mathrm{RT}} \text{ and } \mathbf{v}\,|_{\partial\widehat{\Omega}} = \mathbf{0} \right\} = \left\{ q \in \widehat{Q}_h^{\mathrm{RT}} : \int_{\widehat{\Omega}} q = 0 \text{ and } q(\widehat{\mathbf{x}}_i) = 0,\, i = 1, \cdots, 4 \right\}, \tag{17}$$

where $\mathbf{n}$ denotes the outward unit normal to the boundary of $\widehat{\Omega}$ and $\widehat{\mathbf{x}}_i$, $i = 1, \ldots, 4$ denote its four corners.

Proof. For sake of brevity, we focus only on the proof of (17). The proof of (15) and (16) is a similar to what we present here (a shorter proof of (15) can be obtained as in [19, Proposition 3.1]).

Recall that the mesh $\mathcal{Q}_h$ is obtained from the two vectors $\{\zeta_{1,1}, \ldots, \zeta_{m_1,1}\}$ and $\{\zeta_{1,2}, \ldots, \zeta_{m_2,2}\}$. We name $S_{\alpha,1}^{p}$ and $S_{\alpha+1,1}^{p+1}$ the two uni-variate spline spaces constructed on the first vector, $S_{\alpha,2}^{p}$ and $S_{\alpha+1,2}^{p+1}$ the two uni-variate spline spaces constructed on the second vector, respectively. The dimension of these uni-variate spaces is given in (9)– (10). In particular, we recall that

$$\#S_{\alpha+1,d}^{p+1} = \#S_{\alpha,d}^{p} + 1. \tag{18}$$

From the tensor product structure, we have

$$\#\widehat{Q}_h^{\mathrm{RT}} = \#S_{\alpha,1}^{p} \, \#S_{\alpha,2}^{p}. \tag{19}$$

The inclusion

$$\left\{ \operatorname{div} \mathbf{v} \,:\, \mathbf{v} \in \widehat{V}_h^{\mathrm{RT}} \text{ and } \mathbf{v}\,|_{\partial\widehat{\Omega}} = \mathbf{0} \right\} \subseteq \left\{ q \in \widehat{Q}_h^{\mathrm{RT}} : \int_{\widehat{\Omega}} q = 0 \text{ and } q(\widehat{\mathbf{x}}_i) = 0,\, i = 1, \cdots, 4 \right\},$$

is easy to prove (consider pure tensor velocities $\mathbf{v}$ to get it). Now we have

$$\#\left\{ q \in \widehat{Q}_h^{\mathrm{RT}} : \int_{\widehat{\Omega}} q = 0 \text{ and } q(\widehat{\mathbf{x}}_i) = 0,\, i = 1, \cdots, 4 \right\} = \#\widehat{Q}_h^{\mathrm{RT}} - 5, \tag{20}$$

due to the constraints at the corners and on the mean-value. Taking into account the boundary conditions, (18) and that $\#(S^p_{\alpha,d} \cap H^1_0) = \#S^p_{\alpha,d} - 2$,, we have

$$\begin{aligned} &\#\left\{ \mathbf{v} \,:\, \mathbf{v} \in \widehat{V}_h^{\mathrm{RT}} \text{ and } \mathbf{v}\,|_{\partial\widehat{\Omega}} = \mathbf{0} \right\} \\ &\quad = \#\left((S^{p+1}_{\alpha+1,1} \cap H^1_0) \otimes (S^p_{\alpha,2} \cap H^1_0) \;\times\; (S^p_{\alpha,1} \cap H^1_0) \otimes (S^{p+1}_{\alpha+1,2} \cap H^1_0) \right) \\ &\quad = 2\,\#\widehat{Q}_h^{\mathrm{RT}} - 3\,\#S^p_{\alpha,1} - 3\,\#S^p_{\alpha,2} + 4. \end{aligned} \tag{21}$$

We need in the following

$$\#(S^{p+1}_{\alpha+1,d} \cap H^2_0) = \quad \#S^{p+1}_{\alpha+1,d} - 4 = \#S^p_{\alpha,d} - 3; \tag{22}$$

indeed, from $\operatorname{div} \mathbf{v} = 0 \;\Leftrightarrow\; v = \mathbf{curl}\,\phi$, adding the boundary condition $\mathbf{v}\,|_{\partial\widehat{\Omega}} = \mathbf{0}$ corresponds to the constraint that ϕ is constant on $\partial\widehat{\Omega}$ and has null normal derivative on $\partial\widehat{\Omega}$. Then, ϕ is uniquely determined if we set, e.g., $\phi \in H^2_0(\Omega)$; this yields:

$$\begin{aligned} &\#\left\{ \mathbf{v} \in \widehat{V}_h^{\mathrm{RT}} | \operatorname{div} \mathbf{v} = 0 \text{ and } \mathbf{v}\,|_{\partial\widehat{\Omega}} = \mathbf{0} \right\} = \#\left(S^{p+1,p+1}_{\alpha+1,\alpha+1} \cap H^2_0(\widehat{\Omega}) \right) = \\ &\#(S^{p+1}_{\alpha+1,1} \cap H^2_0)\#(S^{p+1}_{\alpha+1,2} \cap H^2_0) = (\#S^p_{\alpha,1} - 3)(\#S^p_{\alpha,2} - 3) = \\ &\#\widehat{Q}_h^{\mathrm{RT}} - 3\,\#S^p_{\alpha,1} - 3\,\#S^p_{\alpha,2} + 9. \end{aligned} \tag{23}$$

Subtracting (23) from (21), we get

$$\#\left\{ \operatorname{div} \mathbf{v} \,:\, \mathbf{v} \in \widehat{V}_h^{\mathrm{RT}} \text{ and } \mathbf{v}\,|_{\partial\widehat{\Omega}} = \mathbf{0} \right\} = \#\widehat{Q}_h^{\mathrm{RT}} - 5, \tag{24}$$

and then comparing with (20) we finally get (17). □

Theorem 3.1 tells us that if we adopt the pair $\widehat{V}_h^{\mathrm{RT}} \times \widehat{Q}_h^{\mathrm{RT}}$ (14a) in (2), to discretize the Stokes problem (1), an exactly divergence-free velocity field is obtained.

However, one needs to be careful in imposing boundary conditions of Dirichlet type. Actually (14b) tells us that one can impose slip boundary conditions strongly and still get a scheme that is well posed, as long as the corresponding zero mean-value pressure space is adopted (or, the constant pressure is filtered out). On the other hand, the case of no-slip boundary conditions is more tricky. Indeed, according to (17) one should adopt a space of pressures that are null at the four corners of the parametric domain $\widehat{\Omega}$, that is

$$\left\{ q \in \widehat{Q}_h^{\mathrm{RT}} : \int_{\widehat{\Omega}} q = 0 \text{ and } q(\widehat{\mathbf{x}}_i) = 0,\, i = 1, \cdots, 4 \right\}. \tag{25}$$

Such a pressure space ensures stability, but restricts the accuracy of method to first order, to overcome this difficulty, we propose the following two ways to deal with no-slip boundary conditions.

3.2.1 method I

The first approach is based on the following idea: instead of imposing $q(\widehat{\mathbf{x}}_i) = 0$, for the pressure variable q at the four corners $\mathbf{x}_i$, $i = 1, \cdots, 4$, we let the the pressure free at the four corners, that is we adopt the pressure space

$$\left\{ q \in \widehat{Q}_h^{\mathrm{RT}} : \int_{\widehat{\Omega}} q = 0 \right\}. \tag{26}$$

With this choice, (4) holds with a strict inclusion. This leads to a singular problem: indeed the four pressures in (26) that are ortogonal to (25) belong to the kernel of the discrete system, see Figure 3.2.2. To compensate the larger pressure space, system (2) is augmented by four equations involving the four "corner" degrees of freedom for the pressure unknown p_h. These additional equations impose that a component of the momentum is null at the corners, thus ensuring optimality (because of consistency) of the discrete solution and preserving divergence-free velocity;

h	1/8	1/12	1/16	1/20	1/24	1/28	1/32
c_{is}^{RT}	0.195	0.197	0.197	0.197	0.197	0.197	0.197

Table 3: inf-sup test constant c_{is} on the parametric domain for the velocity space $\widehat{V}_h^{\mathrm{RT}}$ with no-slip Dirichlet boundary conditions vs. the T-spline pressure space, $p = 3$ and $\alpha = 2$

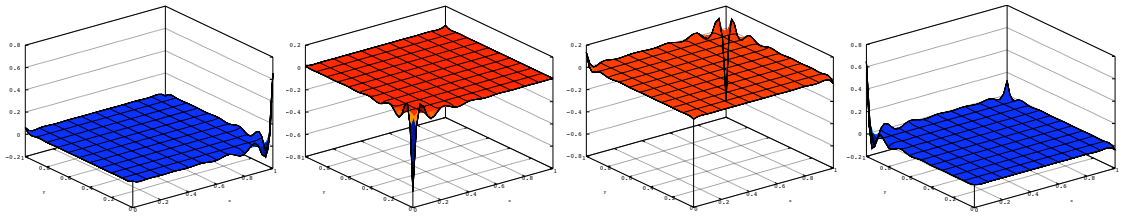

(a) (b) (c) (d)

Figure 1: The four (zero mean-value) pressures of $\widehat{Q}_h^{\mathrm{RT}}(3,2)$ in the kernel of the discrete Stokes system, with no-slip velocity space $\widehat{V}_h^{\mathrm{RT}}(3,2)$

3.2.2 method II

The second approach is based on the construction of a new pressure space $\widetilde{Q}_h^{RT} \subset \widehat{Q}_h^{\mathrm{RT}}$ where the "corner" constraints of (25) are relaxed, while still leaving dimension of the pressure space (25) unchanged. This is done by using *T-splines*, a generalization of B-splines that overcome the tensor-product structure (see [20, 21]). We now briefly detail the construction of the specific T-spline pressure space we are interested in, and we refer to [22] for a general description of T-spline based isogeometric analysis. For the sake of simplicity, we restrict to $p = 3$. In Figure 2(a) we represent the portion of the full tensor product space near one of the corners: each dot, termed "anchor" in the T-spline literature, is associated to a basis function of the space. The first and second coordinate of the anchor are the central knots in the support of the basis function. Figure 2(b) represents the space where the basis function interpolating at the corner is removed (observe that the anchor at the corner is missing); this corresponds to the space (25), which gives only first order approximation in L^2. The optimally accurate T-spline space is obtained removing the anchor and the corresponding vertical edge as depicted in Figure 2(c). Accordingly to the mesh represented in Figure 2(c) (termed *T-mesh*) the four basis functions associated with the green anchors are modified with respect to the corresponding ones of the original tensor-product mesh (Figure 2(a)): indeed, they are constructed from the horizontal knot vector $\Xi := \{0, 0, 0, 0, 2h, 3h, 4h, \ldots, 1\}$ instead of $\Xi := \{0, 0, 0, 0, h, 2h, 3h, 4h, \ldots, 1\}$. The T-spline pressure space guarantees stable coupling with the no-slip velocity space, as shown in the numerical inf-sup test of Table 3.

3.3 Spline spaces on the physical domain

Once the finite dimensional spaces $\hat{V}_h$ and $\widehat{Q}_h$ on the parametric domain $\widehat{\Omega}$ have been defined, we construct the corresponding spaces V_h and Q_h in the physical domain Ω. The pressure space is mapped from the reference domain via the geometrical parametrization $\mathbf{F} : \widehat{\Omega} \longrightarrow \Omega$, that is

$$Q_h = \{q : q \circ \mathbf{F} \in \widehat{Q}_h\}. \tag{27}$$

For the velocity field, we follow two different approaches: the first is to map each component of the velocity variables as scalar fields, that is

$$V_h = \{\, \mathbf{v} \,:\, \mathbf{v} \circ \mathbf{F} \in \hat{V}_h\}, \tag{28}$$

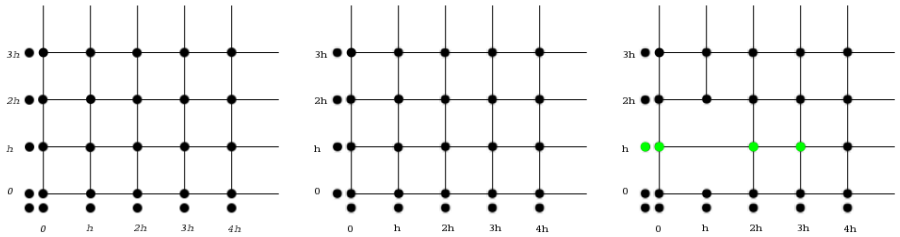

Figure 2: Removal of redundant degrees of freedom of $\widehat{Q}_h^{\mathrm{RT}}$

the other possibility is to use a Piola mapping, which rotates the velocity field

$$V_h = \left\{ \frac{D\,\mathbf{F}}{\det(D\,\mathbf{F})}\,\mathbf{v} \,:\, \mathbf{v} \circ \mathbf{F} \in \hat{V}_h \right\}. \tag{29}$$

In (29), $D\,\mathbf{F}$ is the Jacobian matrix of the parametrization $\mathbf{F}$.

The component-wise mapping (28) is simpler to implement, and gives an isoparametric discrete space when $\mathbf{F}$ is itself a function of the discrete spaces on the reference domain $\widehat{\Omega}$. The Piola mapping, on the other hand, has the advantage of preserving the divergence of the velocity field, and thus preserves the inf-sup stability of the dicrete spaces on the physical domain Ω. Indeed, the numerical tests we have performed demonstrate TH-spaces mapped in both ways preserve stability on the physical domain. On the other hand, RT- (14a) and N-spaces (14b) must be transformed via the Piola mapping since they loose inf-sup stability under the standard isoparametric mapping (28), (see Tab. 5 and Tab. 6). For this reason we define, on Ω, TH-spaces using mapping (28)

$$V_h^{\mathrm{TH}} = \{\, \mathbf{v} \,:\, \mathbf{v} \circ \mathbf{F} \in \widehat{V}_h^{\mathrm{TH}} \}, \tag{30}$$

and RT- and N-spaces usingL mapping (29)

$$V_h^{\mathrm{RT}} = \left\{ \frac{D\,\mathbf{F}}{\det(D\,\mathbf{F})}\,\mathbf{v} \,:\, \mathbf{v} \circ \mathbf{F} \in \widehat{V}_h^{\mathrm{RT}} \right\}, \tag{31}$$

$$V_h^{\mathrm{N}} = \left\{ \frac{D\,\mathbf{F}}{\det(D\,\mathbf{F})}\,\mathbf{v} \,:\, \mathbf{v} \circ \mathbf{F} \in \widehat{V}_h^{\mathrm{N}} \right\}. \tag{32}$$

Furthermore, in order to guarantee optimality of the discrete space, we need $\mathbf{F}$ to be smooth enough compared with the discrete space on the parametric domanin. The condition is that $\gamma_d \geq \alpha_d$, $d = 1, 2$ (see [1], [19]). Notice that this condition is not restrictive, since $\gamma_d \geq 0$ and α_d can be reduced up to $\alpha_d = 0$ by increasing the knot's multiplicity.

4 NUMERICAL EXPERIMENTS

4.1 Examples on the parametric domain

4.1.1 Example with exact solution

As a first numerical experiment we consider problem (1) where we let

$$\Omega \equiv \widehat{\Omega} \tag{33a}$$

and

$$\mu = 1, \quad \mathbf{f} = -\boldsymbol{\nabla}^2\,\bar{\mathbf{u}} + \boldsymbol{\nabla}\bar{p} \tag{33b}$$

h	1/8	1/12	1/16	1/20	1/24	1/28	1/32	1/36	1/40	1/44	1/48
$\|\nabla\mathbf{u} - \nabla\mathbf{u}_h^{RT}\|$	0.000123	3.77e-05	1.62e-05	8.39e-06	4.89e-06	3.1e-06	2.09e-06	1.47e-06	1.07e-06	8.09e-07	6.24e-07
order	-	2.91	2.93	2.95	2.96	2.96	2.97	2.97	2.97	2.98	2.98
$\|p - p_h^{RT}\|$	9.68e-06	1.32e-06	3.69e-07	1.46e-07	6.96e-08	3.75e-08	2.21e-08	1.38e-08	9.1e-09	6.23e-09	4.41e-09
order	-	4.91	4.43	4.17	4.05	4	3.98	3.97	3.97	3.97	3.97
$\|\nabla\mathbf{u} - \nabla\mathbf{u}_h^{N}\|$	9.81e-06	2.07e-06	6.75e-07	2.82e-07	1.38e-07	7.49e-08	4.42e-08	2.78e-08	1.83e-08	1.25e-08	8.87e-09
order	-	3.84	3.89	3.91	3.93	3.94	3.95	3.96	3.96	3.96	3.97
$\|p - p_h^{N}\|$	4.78e-06	1e-06	3.29e-07	1.38e-07	6.76e-08	3.69e-08	2.18e-08	1.37e-08	9.04e-09	6.2e-09	4.4e-09
order	-	3.86	3.87	3.89	3.91	3.92	3.93	3.94	3.95	3.95	3.96
$\|\nabla\mathbf{u} - \nabla\mathbf{u}_h^{TH}\|$	9.41e-06	2e-06	6.59e-07	2.77e-07	1.36e-07	7.4e-08	4.37e-08	2.75e-08	1.81e-08	1.24e-08	8.81e-09
order	-	3.82	3.86	3.89	3.91	3.93	3.94	3.94	3.95	3.95	3.96
$\|p - p_h^{TH}\|$	4.78e-06	1e-06	3.29e-07	1.38e-07	6.76e-08	3.69e-08	2.18e-08	1.37e-08	9.04e-09	6.2e-09	4.4e-09
order	-	3.86	3.87	3.89	3.91	3.92	3.93	3.94	3.95	3.95	3.96

Table 4: Performance of the discretization schemes based on the spaces (14b)–(14c) and on the space $\widehat{V}_h^{\mathrm{RT}} \times \widetilde{Q}_h^{RT}$ for $p = 3$ and $\alpha = 2$ applied to problem (1)-(33)

with

$$\bar{\mathbf{u}} = \begin{bmatrix} (2e^x(-1+x)^2x^2(y^2-y)(-1+2y)) \\ (-e^x(-1+x)x(-2+x(3+x))(-1+y)^2y^2) \end{bmatrix} \tag{33c}$$

$$\begin{aligned} \bar{p} =& (-424 + 156e + (y^2-y)(-456 + e^x(456 + x^2(228 - 5(y^2-y)) + \\ & 2x(-228 + (y^2-y)) + 2x^3(-36 + (y^2-y)) + x^4(12 + (y^2-y))))) \end{aligned} \tag{33d}$$

and we impose the conditions

$$\mathbf{u} = 0 \text{ on } \partial\Omega, \qquad \int_\Omega p = 0. \tag{33e}$$

The unique solution of problem (1)-(33) is clearly given by $(\mathbf{u}, p) = (\bar{\mathbf{u}}, \bar{p})$ Table 4 presents the performance of the discretization schemes based on the spaces (14b)–(14c) and on the space $\widehat{V}_h^{\mathrm{RT}} \times \widetilde{Q}_h^{RT}$ for $p = 3$ and $\alpha = 2$. The results shown indicate optimal rates of convergence for both pressure and velocity.

4.1.2 Rotation of $\widehat{\Omega}$

To clarify the role of the Piola mapping described in Sec. 3.3 we consider a geometrical map $\mathbf{F}$ defining a 90^o around the center of $\widehat{\Omega}$. Athough the image Ω of $\widehat{\Omega}$ under $\mathbf{F}$ coincides in this case with $\widehat{\Omega}$, the component-wise mapping (28) does not preserve the stability of the spaces $\widehat{Q}_h^{\mathrm{RT}} \times \widehat{V}_h^{\mathrm{RT}}$ and $\widehat{Q}_h^{\mathrm{N}} \times \widehat{V}_h^{\mathrm{N}}$ as stated in Sec. 3.3 and shown by the inf-sup test results presented in Tab. 5. This effect is due to the "non-isotropic" nature of these spaces and, indeed, those not affect the space $\widehat{Q}_h^{\mathrm{TH}} \times \widehat{V}_h^{\mathrm{TH}}$ as is also shown in Tab. 5. The results listed in Tab. 6 show that the spaces obtained transforming (14a)-(14c) via the Piola mapping (29) maintain their stability.

4.2 Examples on the physical domain

4.2.1 Driven cavity

To assess the effectiveness of the approach for dealing with no-slip boundary conditions that we we introduced in Sec. 3.2.2 in Sect. 3.2, we apply it to a symmetric "driven cavity" benchmark problem. In this case both components of the velocity are required to vanish on the left and right sides of the boundary of the computational domain $\Omega \equiv (-1, 1) \times (-3, 3)$. At the top ($y = 3$) and bottom ($y = -3$)

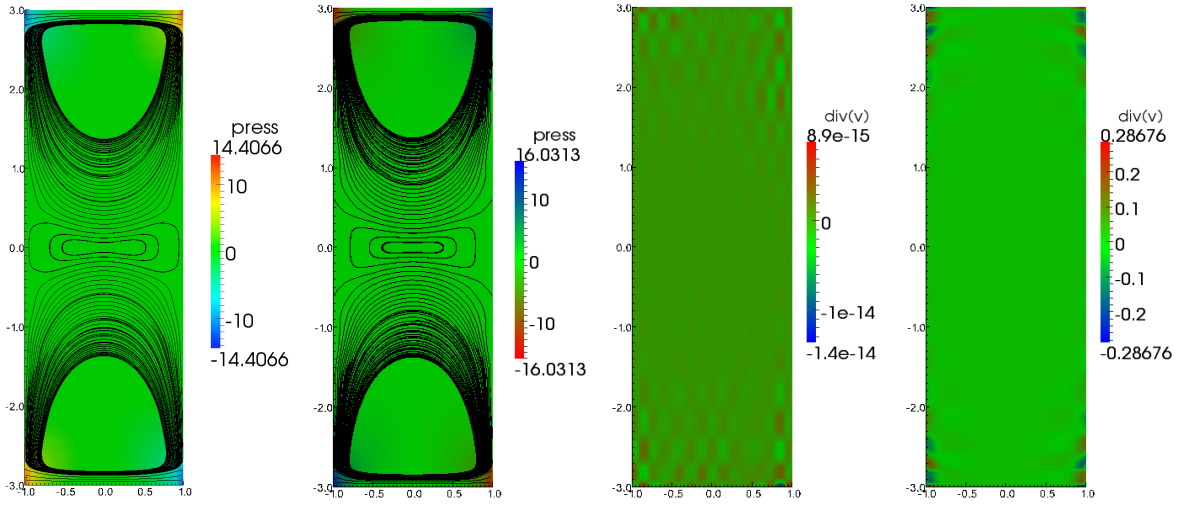

(a) pressure and velocity stremalines, RT-elements using the method of Sec. 3.2.2

(b) pressure and velocity stremalines, TH-elements (14c)

(c) divergence of the velocity, RT-elements using the method of Sec. 3.2.2

(d) divergence of the velocity, TH-elements (14c)

Figure 3: Solution to the driven-cavity problem described in Sect. 4.2.1

	1/8	1/12	1/16	1/20	1/24	1/28	1/32
c_{is}^{RT}	2.48e-08	2.81e-08	4.2e-08	3.47e-08	4.41e-08	3.21e-08	3.08e-08
c_{is}^{N}	0.573	0.446	0.363	0.307	0.266	0.235	0.212
c_{is}^{TH}	0.995	0.995	0.995	0.995	0.995	0.995	0.995

Table 5: inf-sup test constant c_{is} on a rotated physical domain for the spaces (14a)–(14c), with $p = 3$ and $\alpha = 2$, without boundary conditions, transformed via the component-wise mapping (28)

	1/8	1/12	1/16	1/20	1/24	1/28	1/32
c_{is}^{RT}	0.879	0.883	0.884	0.884	0.884	0.884	0.884
c_{is}^{N}	0.971	0.972	0.973	0.973	0.973	0.973	0.973
c_{is}^{TH}	0.995	0.995	0.995	0.995	0.995	0.995	0.995

Table 6: inf-sup test constant c_{is} on a rotated physical domain for the spaces (14a)–(14c), with $p = 3$ and $\alpha = 2$, without boundary conditions, transformed via the Piola mapping (29)

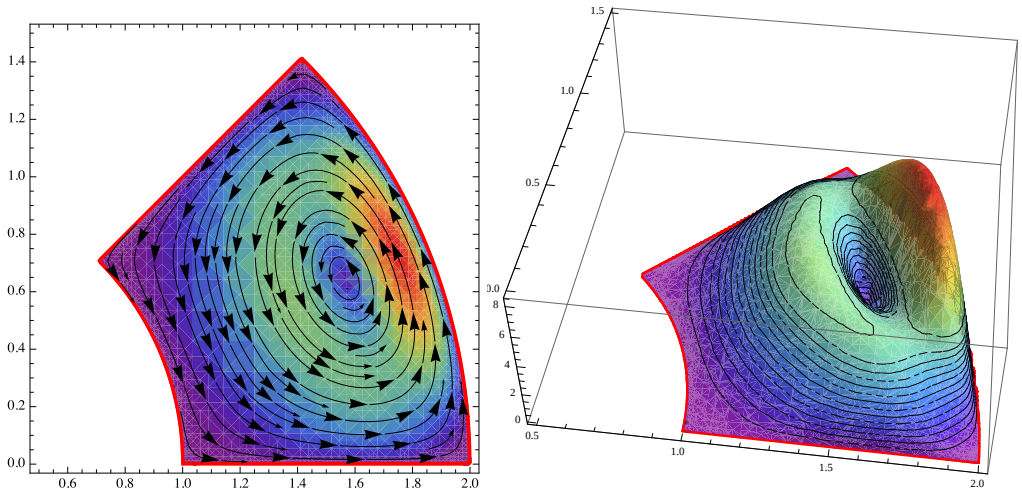

(a) Velocity streamlines (b) Modulus of velocity

Figure 4: Domain geometry and velocity component of the exact solution

sides it is required to be directed in the positive and nrgative x direction, respectively and to have unitary magnitude. This benchmark is known to induce dramatic failures in unstable formulations due to the pressure singularities in the two top corners of the domain. The solution computed with $p = 3$ and $\alpha = 2$ and a mesh-step $h = \frac{1}{16}$ is shown in Fig. 3(a) and displays no spurious oscillations. Also shown for comparison in (14c) is the solution computed with the TH-elements, while Figs. 3(c) and 3(a) depict the divergence of the velocity field computed the RT and TH spaces respectively, which is null (apart from floating-point truncation errors) in the former case (Fig 3(c)) as expected.

4.2.2 Problem with vanishing velocity on the boundary

As a first example with $\Omega \neq \widehat{\Omega}$ we consider a problem set on a simple NURBS geometry and with no-slip boundary conditions on the whole domain boundary. The geometry of the domain Ω and the velocity part of the exact solution are depicted in Fig. 4. The results presented in Tab. 7 show the convergence rates of the numerical solutions computed using the discrete spaces (27)-(30), (27)-(32) and for the space obtained by combining the T-spline pressure space $\widetilde{Q}_h$ transformed via (27) and the velocity space (31). The results shown indicate optimal rates of convergence for both pressure and velocity.

4.2.3 Fluid-Structure interaction example

The final test case we present is a preliminary example of fluid-structure interaction. An infinitely long cylinder c_r of radius r and center $\mathbf{x}_r$ filled with a solid material of density ρ_r is placed in middle of a cylinder of radius $R > r$ and center $\mathbf{x}_R$ filled with a fluid of viscosity μ and density ρ_R. The cylinder c_r moves under the effect of gravity, of the fluid pressure on its surface and of an additional force $\mathbf{f}_\mathbf{x} = k(\mathbf{x}_R - \mathbf{x}_r)$. Exploiting the symmetry of the problem we can use as a simulation domain Ω only half of the fluid domain as depicted in Fig. 6(a), we impose no-slip boundary conditions on the portions of $\partial\Omega$ denoted as Γ_r and Γ_R in that figure and that the horizontal component of the velocity

h	1/8	1/12	1/16	1/20	1/24	1/28	1/32	1/36	1/40	1/44	1/48
$\|\nabla \mathbf{u} - \nabla \mathbf{u}_h^{RT}\|$	0.378	0.118	0.0516	0.027	0.0159	0.0101	0.00685	0.00485	0.00356	0.00268	0.00208
order	-	2.87	2.88	2.9	2.91	2.92	2.93	2.94	2.94	2.95	2.95
$\|p - p_h^{RT}\|$	0.00836	0.000905	0.000205	6.74e-05	2.76e-05	1.31e-05	6.89e-06	3.93e-06	2.39e-06	1.52e-06	1.01e-06
order	-	5.48	5.15	5	4.9	4.84	4.8	4.76	4.73	4.71	4.69
$\|\nabla \mathbf{u} - \nabla \mathbf{u}_h^{N}\|$	0.0347	0.00797	0.00273	0.00118	0.000586	0.000324	0.000193	0.000123	8.13e-05	5.61e-05	3.99e-05
order	-	3.63	3.72	3.78	3.82	3.84	3.86	3.88	3.89	3.9	3.91
$\|p - p_h^{N}\|$	0.000307	3.78e-05	8.25e-06	2.5e-06	9.35e-07	4.06e-07	1.97e-07	1.04e-07	5.84e-08	3.47e-08	2.16e-08
order	-	5.16	5.3	5.35	5.39	5.41	5.43	5.44	5.44	5.45	5.46
$\|\nabla \mathbf{u} - \nabla \mathbf{u}_h^{TH}\|$	0.0325	0.0075	0.00258	0.00111	0.000557	0.000309	0.000185	0.000117	7.77e-05	5.36e-05	3.82e-05
order	-	3.61	3.71	3.77	3.8	3.83	3.85	3.87	3.88	3.89	3.9
$\|p - p_h^{TH}\|$	8.85e-05	1.08e-05	2.4e-06	7.36e-07	2.79e-07	1.22e-07	5.96e-08	3.16e-08	1.79e-08	1.07e-08	6.67e-09
order	-	5.18	5.24	5.29	5.33	5.35	5.37	5.39	5.4	5.41	5.42

Table 7: Performance of discretizations based on the spaces (14a)–(14c), with $p = 3$ and $\alpha = 2$

vanish on Γ_s. The complete system to be solved reads

$$\begin{cases} \dot{\mathbf{v}}_r(t) = \dfrac{1}{\rho_r \pi r^2} \left(k(\mathbf{x}_r(t) - \mathbf{x}_R) + \displaystyle\int_{\Gamma_r} p(t, \mathbf{x})\ \mathbf{n} \right) - \mathbf{g} \\ \dot{\mathbf{x}}_r(t) = \mathbf{v}_r(t) \\ \mathbf{x}_r(0) = \bar{\mathbf{x}}_r,\ \mathbf{v}_r(0) = \bar{\mathbf{v}}_r \end{cases} \tag{34a}$$

$$\begin{cases} -\mu\ \boldsymbol{\nabla}^2\, \mathbf{u}\,(t, \mathbf{x}) + \dfrac{1}{\rho_R} \boldsymbol{\nabla} p(t, \mathbf{x}) = \mathbf{g} & \text{in } \Omega(t) \\ \boldsymbol{\nabla} \cdot\ \mathbf{u}\,(t, \mathbf{x}) = 0 & \text{in } \Omega(t) \\ \mathbf{u}\,(t, \mathbf{x}) = 0 & \text{on } \Gamma_R \\ \mathbf{u}\,(t, \mathbf{x}) \cdot \mathbf{n} = 0 & \text{on } \Gamma_s(t) \\ \mathbf{u}\,(t, \mathbf{x}) = \mathbf{v}_r(t) & \text{on } \Gamma_r(t). \end{cases} \tag{34b}$$

To solve (34) numerically, we discretize (34a) in time via a semi-implicit Euler scheme where only the term containing the fluid pressure is treated explicitely, so that at each time step (34a) is solved first to determine the position and velocity of c_r, and thus the shape of $\Omega(t)$, and then (34b) can be solved to update the force acting c_r. The results shown in Fig. 5 correspond to the values of the parameters listed in Tab. 6(b)

Acknowledgements

This research was supported by the European Research Council through the FP7 Ideas Starting Grant program GeoPDEs Innovative compatible discretization techniques for Partial Differential Equations.

References

[1] Bazilevs Y, Beirão da Veiga L, Cottrell J, Hughes T, Sangalli G. Isogeometric analysis: approximation, stability and error estimates for h-refined meshes. *Math. Models Methods Appl. Sci.* 2006; **16**:1031–1090.

[2] Bressan A. Elementi isogeometrici per il problema di stokes. Master's Thesis, Università di Pavia 2009.

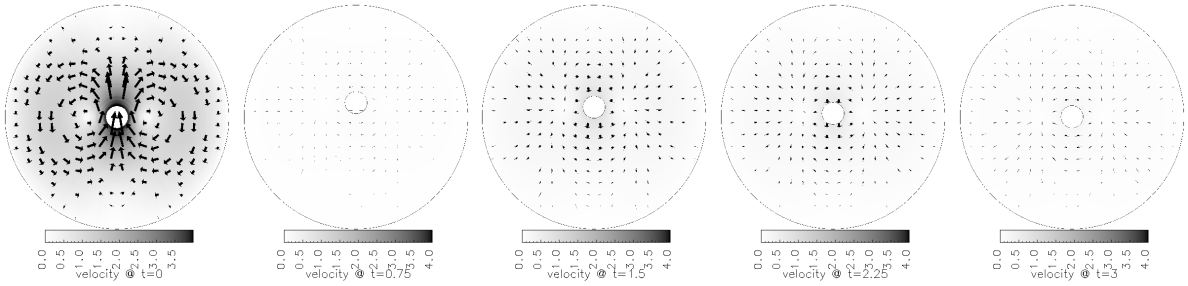

(a) Velocity snapshots computed with the RT discretization

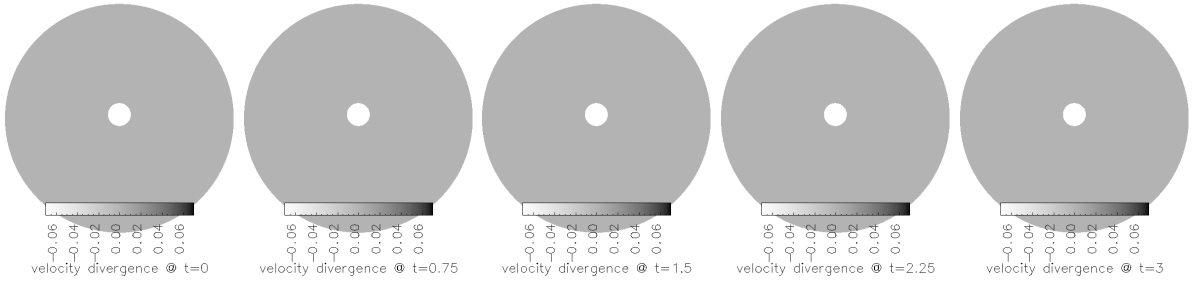

(b) Divergence of the velocity computed with the RT discretization

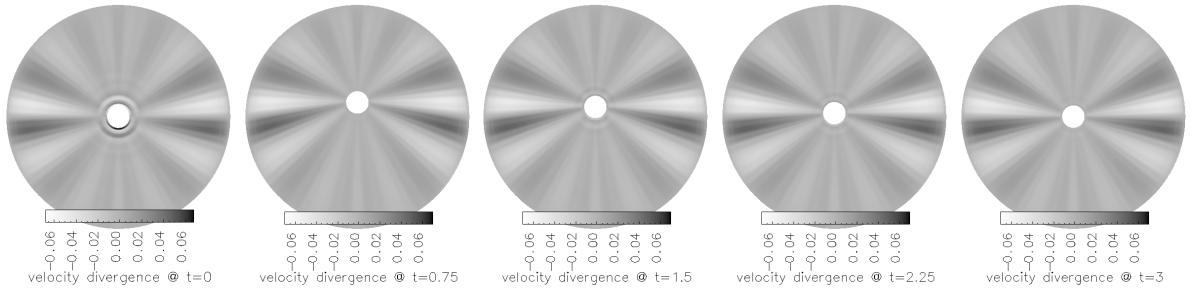

(c) Divergence of the velocity computed with the TH discretization

Figure 5: Moving Cylinder

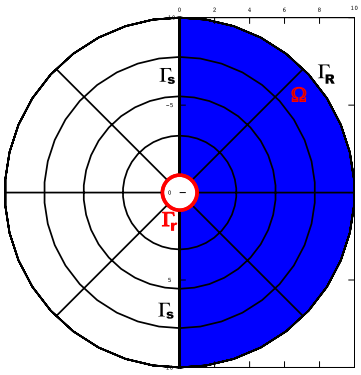

(a) Computational domain and grid for the moving cylinder example

r	R	ρ_r	ρ_R	μ	$\bar{\mathbf{x}}_r$	$\bar{\mathbf{v}}_r$
1	10	1	1	3	$\mathbf{x}_R$	3

(b) Parameters for the simulation of Fig. 5

Figure 6: data for the moving cylinder problem

[3] Auricchio F, Beirão da Veiga L, Buffa A, Lovadina C, Reali A, Sangalli G. A fully "locking-free" isogeometric approach for plane linear elasticity problems: a stream function formulation. *Comput. Methods Appl. Mech. Engrg.* 2007; **197**(1-4):160–172.

[4] Hughes TJR, Cottrell JA, Bazilevs Y. Isogeometric analysis: Cad, finite elements, nurbs, exact geometry and mesh refinement. *Computer Methods in Applied Mechanics and Engineering* 2005; **194**(39-41):4135 – 4195, doi:DOI: 10.1016/j.cma.2004.10.008.

[5] Brezzi F, Fortin M. *Mixed and Hybrid Finite Element Methods*. Springer: New York, 1991.

[6] Gerbeau J, Bris CL, Bercovier M. Spurious velocities in the steady flow of an incompressible fluid subjected to external forces. *Int. Jour. Num. Meth. Fluids* 1997; **25**:679–695.

[7] Christon MA. The consistency of pressure-gradient approximations used in multi-dimensional shock hydrodynamics. *International Journal for Numerical Methods in Fluids* 2009; .

[8] Carrero J, Cockburn B, Schötzau D. Hybridized globally divergence free LDG methods. part I: the Stokes problem. *Mathematics of Computation* 2005; **75**(254):533–563.

[9] Cockburn B, Kanschat G, Schötzau D. A locally conservative LDG method for the incompressible Navier–Stokes equations. *Mathematics of Computation* 2004; **74**(251):1067–1095.

[10] Taylor C, Hood P. A numerical solution of the Navier-Stokes equations using the finite element technique. *Internat. J. Comput. & Fluids* 1973; **1**(1):73–100.

[11] Nedelec J. A new family of mixed finite elements in 3. *Numerische Mathematik* 1986; **50**(1):57–81.

[12] Raviart P, Thomas J. A mixed finite element method for 2nd order elliptic problems. *Mathematical Aspects of the Finite Element Method, Lecture Notes in Mathematics* ; **606**:292–315.

[13] de Boor C. *A practical guide to splines*, *Applied Mathematical Sciences*, vol. 27. Revised edn., Springer-Verlag: New York, 2001.

[14] Nedelec J. Mixed finite elements in 3. *Numerische Mathematik* 1980; **35**(3):315–341.

[15] Cockburn B, Kanschat G, Schötzau D. A note on discontinuous Galerkin divergence-free solutions of the Navier-Stokes equations. *J. Sci. Comput.* 2007; **31**(1-2):61–73.

[16] Cockburn B, Kanschat G, Schwab C. Local discontinuous galerkin methods for the stokes system. *SIAM Journal on Numerical Analysis* 2003; **40**(1):319–343.

[17] Austin TM, Manteuffel TA, McCormick S. A robust multilevel approach for minimizing $\mathbf{H}$(div)-dominated functionals in an $\mathbf{H}^1$-conforming finite element space. *Numer. Linear Algebra Appl.* 2004; **11**(2-3):115–140.

[18] Kanschat G. A continuous finite element de rham complex and its application to the two-dimensional stokes problem 2009.

[19] Buffa A, Sangalli G, Vázquez R. Isogeometric analysis in electromagnetics: B-splines approximation. *Comput. Methods Appl. Mech. Engrg.* 2009; (in press).

[20] Sederberg T, Zheng J, Bakenov A, Nasri A. T-splines and t-nurccs. *ACM SIGGRAPH 2003 Papers*, ACM, 2003; 484.

[21] Sederberg T, Cardon D, Finnigan G, North N, Zheng J, Lyche T. T-spline simplification and local refinement. *ACM Transactions on Graphics (TOG)* 2004; **23**(3):276–283.

[22] Bazilevs Y, Calo V, Cottrell J, Evans J, Hughes T, Lipton S, Scott M, Sederberg T. Isogeometric analysis using t-splines. *Computer Methods in Applied Mechanics and Engineering* 2009; .